Anisotropic molecular photoemission dynamics: Wigner time delay versus time delay from RABBIT measurements

Morgan Berkane, Antoine Desrier, Camille Lévêque, Richard Taïeb, Jérémie Caillat

▶ To cite this version:

Morgan Berkane, Antoine Desrier, Camille Lévêque, Richard Taïeb, Jérémie Caillat. Anisotropic molecular photoemission dynamics: Wigner time delay versus time delay from RABBIT measurements. Physical Review A, 2024, 109 (1), pp.013101. ⟨10.1103/PhysRevA.109.013101⟩. ⟨hal-04380631⟩

HAL Id: hal-04380631
https://hal.sorbonne-universite.fr/hal-04380631v1

Submitted on 11 Jan 2024

PHYSICAL REVIEW A **109**, 013101 (2024)

Anisotropic molecular photoemission dynamics: Wigner time delay versus time delay from RABBIT measurements

Morgan Berkane, Antoine Desrier, Camille Lévêque, Richard Taïeb, and Jérémie Caillat[*]
Sorbonne Université, CNRS, Laboratoire de Chimie Physique-Matière et Rayonnement, LCPMR, F-75005 Paris, France

(Received 12 October 2023; accepted 5 December 2023; published 8 January 2024)

We investigate signatures of anisotropy on the dynamics of time-resolved near-threshold molecular photoemission through simulations on a one-dimensional asymmetric model molecule. More precisely, we study the relationship between the fundamental Wigner delays that fully characterizes the dynamics of one-photon ionization and the delays inferred from two-color interferometric RABBIT measurements. Our results highlight two different properties pertaining to each of these delays. The first one is related to the inherent necessity to set an arbitrary electron position origin to define and compute the Wigner delay. The second one is the dependency of the RABBIT delay on the frequency of the probe laser. Our results show that the angular variations of both delays converge for a specific choice of the position origin and in the limit of a vanishing infrared probe frequency.

DOI: 10.1103/PhysRevA.109.013101

I. INTRODUCTION

The tools of attoscience have allowed revisiting the process of photoemission in the time domain since the late 2000s [1–4]. The ultrafast dynamics revealed by these studies, commonly addressed in terms of scattering time delays [5], range from a few femtoseconds (fs) down to few attoseconds (as). These pioneering experimental studies were carried out using the reconstruction of attosecond beatings by interferences of two-photon transitions (RABBIT) [6–9] and streaking [10] schemes, that were initially conceived for the temporal characterization of attosecond light sources [11]. Both can be seen as interferometric pump-probe schemes where a photoemission process is triggered by an attosecond light pulse in the extreme ultra violet (XUV) regime, and coherently probed by a synchronized infrared (IR) field. As attosecond science evolved towards atto*chemistry* [12], the dynamics of photoemission have been investigated in more elaborate molecular systems and nanostructures [13–19], including chiral species [20].

This puts forward essential issues regarding an increasing number of degrees of freedom, among which is the anisotropy of attosecond-resolved photoemission dynamics [21–23]. This anisotropy was first raised in numerical experiments on a model CO molecule where orientation-resolved photoemission dynamics were probed using the streaking scheme [24]. These simulations, spanning photoelectron energies up to ∼80 eV, evidenced "stereo" delays reaching up to several tens of as. The stereo streaking delays simulated in this work match accurately the angular variations of the actual scattering delays over most of the covered energy range. However, discrepancies showing up at lower energies, below ∼20 eV, suggest a significant influence of the probe in the measured temporal asymmetries. Indeed, measurements of photoemission delays in He atoms using RABBIT [25] have highlighted the symmetry breakdown induced by the two-photon probe process itself [26–28]. Orientation-resolved RABBIT experiments further evidenced the imprint of the initial and final states asymmetry on photoemission dynamics in Ar atoms [29] and dimers [30]. The first experiments reporting anisotropic molecular photoemission dynamics were also performed on CO, using RABBIT in the 0–20 eV photoelectron energy range [31]. The results are consistent with the streaking simulations of Ref. [24], evidencing an anisotropy reaching several tens of as, with "faster" photoemission from either the C or O side of the molecule depending on the photoelectron energy. By comparing photoemission from different electronic channels, this work evidenced experimental imprints of the initial electron position within the molecule in the measured orientation-dependent delays [32]. In the same spirit, resonant asymmetric photoemission delays were recently investigated experimentally in NO [33], also using RABBIT but with improved angular resolution. These measurements evidence delays varying by few to several tens of as when scanning the photoemission angle in the molecular frame, within the 20–40 eV energy range. In Ref. [34], numerical RABBIT simulations on model molecules similar to the one used in Ref. [24] evidenced a probe-induced asymmetry of the measured delays amounting to up to 100 as near-ionization threshold, and persisting significantly over several tens of eV. These large values were attributed to the choice of the origin in the definition of the Wigner delays.

Beyond the fundamental time-domain interpretation of photoemission scattering delays [2,35], the question of their measurement and notably of the influence of the probe in attosecond pump-probe experiments, has been the subject of an important theoretical activity, see, e.g., Refs. [36–41]. However, available analytical models to date accurately predict the dependency of the measurements with respect to probe parameters such as the wavelength, but none account explicitly for the anisotropy of the pertubation induced by the measurement.

In this paper, we clarify the role of the arbitrary origin in the definition and computation of Wigner delays and study

---

[*] jeremie.caillat@sorbonne-universite.fr

the imprint of the average initial electron position in delays measured using the RABBIT technique. This indirectly raises issues regarding the role of the probe wavelength in RABBIT measurements. Our work is based on numerical simulations performed on a one-dimensional (1D) asymmetric model molecule. The paper is organized as follows. The model molecule is presented in Sec. II. The influence of the electron position origin on the orientation-resolved Wigner scattering delay is investigated in Sec. III and the influence of the probe wavelength in orientation-resolved RABBIT measurements independently in Sec. IV. Eventually, we address in Sec. V the anisotropic differences between the fundamental Wigner delays and RABBIT measurements, which inherit the origin-dependency of the first and the wavelength-dependency of the second.

By default, equations are expressed in atomic units (a.u.).

II. NUMERICAL TOOLBOX

A. Model molecule

We performed our simulations on a 1D model molecule, reminiscent of the ones used, e.g., in Refs. [24,34]. It is made of a single active electron initially bound to an asymmetric effective potential. Its Hamiltonian reads

$$H_0 = -\frac{1}{2}\frac{\partial^2}{\partial x^2} + V_{\text{N-e}}(x), \tag{1}$$

where x is the electron coordinate and

$$V_{\text{N-e}}(x) = -\frac{q}{\sqrt{(x-X_1)^2+a^2}} - \frac{(1-q)}{\sqrt{(x-X_2)^2+a^2}} \tag{2}$$

is an asymmetric double soft-core potential. The parameters X_1, X_2 represent the (fixed) positions of the nuclei, q is an effective atomic charge, and a is an arbitrary screening constant. This set of parameters are numerical knobs that can be tuned to assign the model some desired properties. Here we set the charge q to 0.33 a.u. and the internuclear distance $R = |X_2 - X_1|$ to 1.115 Å. The screening parameter ($a = 0.198$ Å) was adjusted to obtain an ionization potential $E_\text{i} = 29.77$ eV. The resulting potential function is shown in Fig. 1(a). It was thus designed with some arbitrariness to obtain realistic molecular features, and more specifically, to reflect the difference of electronegativity between the two atoms in a heteronuclear molecule. The asymmetry is reflected in the ground-state wave function $\Phi_0(x)$, also displayed in Fig. 1(a), which is the initial state in all the simulations presented hereafter.

B. 1D polar coordinates

In the present work, we solved the time-independent Schrödinger equation (see, e.g., Sec. III A) using a partial-wave expansion consisting in expressing any function of $x \in \mathbb{R}$ in terms of its odd and even components. It relies on 1D "polar" coordinates for the electron position, namely, a radius $r = |z| \in \mathbb{R}^+$ and an angle $\theta = \arccos(z/|z|) \in \{0^\circ, 180^\circ\}$, where $z = x - x_\text{ref}$ is the "cartesian" coordinate x referred to an arbitrary origin x_ref. More details about this approach are provided in the Appendix. This technical choice has no practical consequence on the results presented hereafter, which are numerically converged. Nevertheless, it tightens the analogies between the present work and the usual approaches invoked in three dimensions (3D), see, e.g., [14]. As will be discussed further, it highlights the arbitrariness of the origin of the partial wave expansion, i.e., the origin x_ref chosen here to discriminate the right and left sides of the molecule.

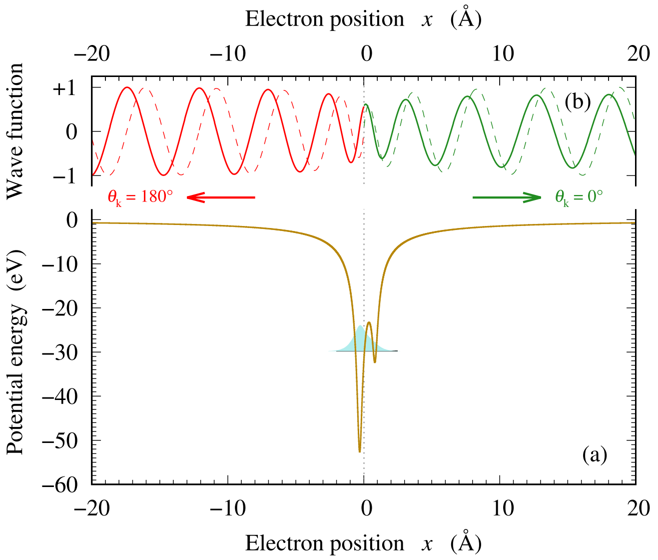

FIG. 1. One-dimensional model molecule. (a) Electron-nuclei potential $V_{\text{N-e}}(x)$ as a function of the electron position x (dark yellow full curve). The ground-state electronic wave function is also shown (light blue filled curve). (b) Electronic continuum wave function (full curve) selected at the energy $\varepsilon = 4.35$ eV by a one-photon transition from the electronic ground state. Odd-parity reference wave function (dashed curve) used to define and compute the orientation-dependent phase shifts. The displayed continuum wave functions are normalized such that their amplitudes asymptotically converge to 1 on the left-hand side of the molecule. In this figure, the left or right discrimination and the parity refer to the arbitrary $x = 0$ position (indicated by a vertical dotted line).

All through the paper, θ_k represents the direction of photoemission, restricted to two discrete values $\theta_\text{k} = 0^\circ$ (emission towards the right, $x > 0$) and 180° (towards the left, $x < 0$).

III. FUNDAMENTAL DYNAMICS: ANISOTROPIC WIGNER DELAYS

We first studied how the asymmetry of the model molecule is reflected in the so-called stereo Wigner delays [24,31], i.e., the relative photoelectron scattering delay towards one side of the molecule (here left) in comparison to the other (right).

A. Selected continuum wave function

To this end, we computed and analyzed the continuum-wave functions selected by one-photon ionization processes (SCWF). The SCWF formalism [42] is a convenient approach which unambiguously separates the computation of electronic continuum wave functions in the framework of photoemission from their analysis in terms of scattering dynamics. For a given transition leading to a final energy ε, the selected continuum state is defined in 1D as

$$|\Psi_{\varepsilon,\text{sel}}\rangle = \sum_{k=1,2} \langle \Psi_{\varepsilon,k}|\hat{d}|\Phi_0\rangle |\Psi_{\varepsilon,k}\rangle, \tag{3}$$

TABLE I. Orientation-resolved Wigner delays $\tau_{\rm w}(\theta_{\rm k})$ [Eq. (4)] computed at $\varepsilon = 4.35$ eV for three values of the reference position $x_{\rm ref}$ arbitrarily discriminating the right ($\theta_{\rm k} = 0^\circ$) and left ($\theta_{\rm k} = 180^\circ$) sides of the asymmetric model molecule.

$x_{\rm ref}$ (Å)	−0.20	+0.00	+0.20
$\tau_{\rm w}(0^\circ)$ (as)	+15.6	−0.5	−16.5
$\tau_{\rm w}(180^\circ)$ (as)	−8.9	+7.2	+23.3

where $|\Phi_0\rangle$ is the initial bound state, $\hat{d}$ is the dipole operator associated with the process, and $\{|\Psi_{\varepsilon,1}\rangle, |\Psi_{\varepsilon,2}\rangle\}$ is an *arbitrary* orthonormal eigenstate basis for the doubly degenerate continuum at the considered energy.

As an illustration, the SCWF computed for $\varepsilon = 4.35$ eV (full curve) is shown in Fig. 1(b). It corresponds to an ionization triggered by a 35.67-eV photon, i.e., the 21st harmonic of a 800-nm IR laser. Photoemission dynamics are encoded in the spectral variations of the phases of its asymptotic oscillations [42]. The origin chosen to discriminate the right and left sides of the molecule is here the origin of the x axis (i.e., $x_{\rm ref} = 0$), which is itself arbitrary.

B. Orientation-resolved Wigner phase shifts and delays

The orientation-dependent phase shifts of the SCWF, $\eta(\theta_{\rm k})$, are defined and computed with respect to an arbitrary intermediate reference wave at the same energy. For the latter, we took the radial s Coulomb wave of the hydrogen atom centered at $x = x_{\rm ref}$, displayed as a dashed curve in Fig. 1(b). This is a typical choice to characterize photoemission dynamics in terms of delays since molecular continuum waves behave asymptotically as Coulomb waves. Note that these phase shifts depend *by definition* on the origin $x_{\rm ref}$ chosen to discriminate the left and right sides of the molecule, or, in other words to set up the 1D partial-wave expansion in terms of even and odd components when computing the SCWF, see the Appendix.

The orientation-resolved Wigner delays are then defined as the group delay

$$\tau_{\rm w}(\theta_{\rm k}) = \frac{\partial \eta(\theta_{\rm k})}{\partial \varepsilon}. \tag{4}$$

When computing them, among a series of numerical tests, we ensured that the phase shifts were evaluated in a region where they do not depend on their computation distance on either side of the origin, i.e., in the asymptotic region where the potential is symmetric. However, they naturally inherit the $x_{\rm ref}$ dependency from $\eta(\theta_{\rm k})$. The dependency of the Wigner delays with respect to this analysis parameter is illustrated in Table I, with the values of $\tau_{\rm w}(\theta_{\rm k})$ obtained at $\varepsilon = 4.35$ eV for $x_{\rm ref} = -0.20$, 0, and +0.20 Å, respectively. With these data, one can verify that shifting the origin from 0 to a given value $x_{\rm ref}$ is equivalent to modifying the path difference between the photoelectron and the arbitrary intermediate reference by $-x_{\rm ref}$ on the right side and $+x_{\rm ref}$ on the left side. Indeed, it induces a delay shift on each side of the molecule which can be accurately modeled as [31,32]

$$\delta\tau_{\rm w}(\theta_{\rm k}) = \cos\theta_{\rm k}\frac{x_{\rm ref}}{\sqrt{2\varepsilon}}, \tag{5}$$

i.e., the time needed for an electron with constant velocity $\sqrt{2\varepsilon}$ to cover the path difference $\delta x = +x_{\rm ref}$ towards the left or $-x_{\rm ref}$ towards the right.

Our simulations covered photoelectron energies ranging over ~10 eV near threshold. The obtained orientation-resolved delays towards the left and right sides of the molecule are displayed in Figs. 2(a), and 2(b), respectively, for a series of $x_{\rm ref}$ values comprized between −0.20 and +0.20 Å. They typically lie in the attosecond range. It is noteworthy that such small, sub-Å, displacements of the origin (which here remain "within" the molecule) induce considerably large relative variations of the delays, with no converging pattern [see the linear dependency given by Eq. (5)].

These orientation-resolved delays depend not only on an arbitrary origin, but also on the nature of a reference system (here Coulomb waves), which is also arbitrary. This last dependency nevertheless vanishes when considering the stereo-Wigner delays [24,31,34], defined here as the difference

$$\Delta\tau_{\rm w} = \tau_{\rm w}(180^\circ) - \tau_{\rm w}(0^\circ). \tag{6}$$

Figure 3 shows the values of $\Delta\tau_{\rm w}$ obtained with the orientation-resolved delays commented above (Fig. 2). They are here of the same order of magnitude than the delays $\tau_{\rm w}(\theta_{\rm k})$ themselves. We verified with a few test cases that these values remain unchanged when using intermediate reference plane waves instead of Coulomb waves. However, the $x_{\rm ref}$ dependency remains just as pronounced as for the orientation-resolved delays.[1]

The linear dependency of the stereo Wigner delay with respect to the origin, which is considered to be the main cause for the channel-dependent delay variations reported in Ref. [31], is inherent to its very definition. In practice, the most natural choice consists in setting the origin to the average electron position in the initial state

$$\langle x\rangle_0 = \int_{-\infty}^{+\infty} x|\Psi_0(x)|^2\, dx. \tag{7}$$

Characterizing the initial state with this average position is as relevant as characterizing the photoemission dynamics, in the final state, in terms of group delays.[2] Here, $\langle x\rangle_0 = -0.16$ Å.

---

[1] It is important to note that the origin dependency concerns only the orientation-dependent (or partial-wave) *analysis* of the SCWF, but not the SCWF itself which is by essence origin invariant. It therefore impacts the phase shifts and the associated group delays, but not observables such as the orientation-dependant ionization *probabilites* (which are proportional to the squared asymptotic amplitudes of the SCWF on each side of the molecule [42]).

[2] The question of the origin-dependency is generally overlooked in studies dealing with atoms or centrosymmetric molecules, including in standard textbooks on scattering theory, where it is "naturally," implicitly and undisputedly set at the center of symmetry for obvious practical reasons.

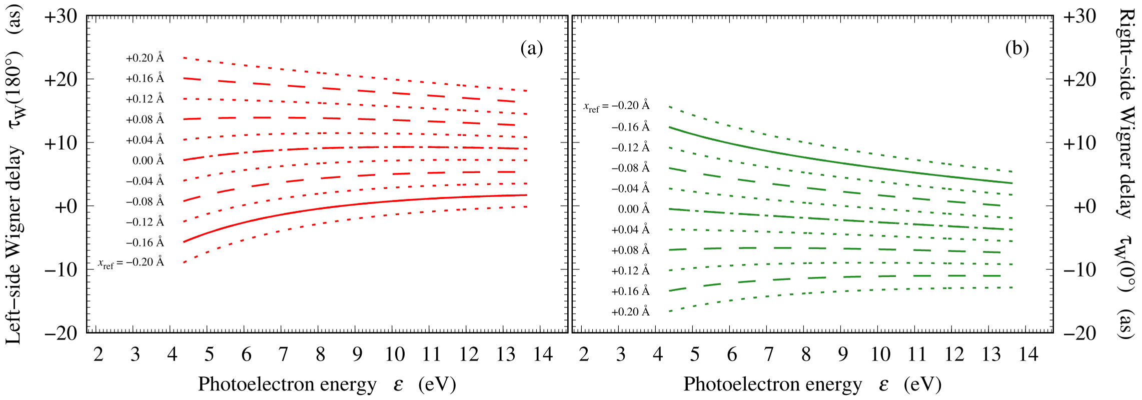

FIG. 2. Orientation-resolved Wigner delays [Eq. (4)] towards the (a) left and (b) the right sides of the molecule as a function of the photoelectron energy. The data are displayed for a set of reference positions $x_{\rm ref}$ discriminating the left and right sides of the molecule. The delays are defined with respect to Coulomb waves centered at $x_{\rm ref}$. The $x_{\rm ref} = 0$ results (dashed-dotted curve) were obtained through SCWF computations and analysis (see text) and were used to infer the $x_{\rm ref} \neq 0$ results (alternating line styles, see labels) using the ε- and $x_{\rm ref}$-dependent correction given in Eq. (5). The full curves correspond to the data obtained for $x_{\rm ref} = \langle x \rangle_0$ [see Eq. (7)].

The corresponding data in Figs. 2 and 3 are displayed in full lines.

This arbitrary choice is also comforted by theoretical studies regarding particle scattering in 1D anisotropic potentials [43]. Nevertheless, it remains to be confronted to the context in which the stereo Wigner delays are investigated experimentally, using interferometric schemes based on the RABBIT [8] and streaking [10] setups. In the present work, we focus on the RABBIT approach, as discussed below.

IV. RABBIT SIMULATIONS: ANISOTROPIC MOLECULAR DELAYS

In this section, we investigate the anisotropic photoemission dynamics inferred from RABBIT measurements. This part is *a priori* independent of the previous section since, as we will see, the dependencies of the "RABBIT delays" are fundamentally different from the one discussed for the Wigner delays. Following the RABBIT scheme, we simulated photoemission from our asymmetric model molecule with a comb of XUV odd harmonics of an IR laser, dressed by the fundamental field with frequency ω_0. We solved numerically the time-dependent Schrödinger equation (TDSE) starting from the ground state, the dipole interaction with the XUV, and IR pulses being implemented in the velocity gauge. The light pulse vector potentials were all assigned $\sin^2$ temporal profiles lasting 40 fs (15 periods of a 800-nm laser, full durations). The harmonics were synchronized with no "attochirp," for the sake of simplicity, but were time shifted by an adjustable delay $\tau_{\text{XUV-IR}}$ with respect to the IR pulse (relative to their maxima). We set the intensities safely in the perturbative regime, notably to prevent any significant transitions involving more than one IR photon.

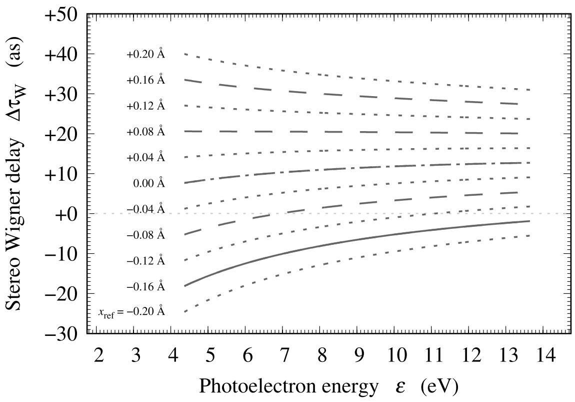

FIG. 3. Stereo Wigner delays $\Delta\tau_{\rm w}$ [Eq. (6)] as a function of the photoelectron energy ε, computed for a set of reference positions $x_{\rm ref}$, see caption of Fig. 2.

A. Photoelectron spectra

Orientation-resolved photoelectron spectra were computed using narrow spectral filters [44] applied to the left and right sides of the wave function at the end of the simulations. To safely discriminate photoelectrons leaving towards each side of the molecule, we let the wave function propagate a few fs after the end of the pulses. In the present context, we emphasize that these spectra do not depend on the origin set to discriminate the right and left sides of the molecule, consistently with their experimental equivalent.

The spectra consist in a series of main peaks (HA_{2q+1}), evenly separated by a $2\omega_0$ energy gap, associated with the absorption of each harmonic. Additional sidebands, each induced by two-photon transitions involving one harmonic and one IR photon, show up in between. Each sideband (SB_{2q}) results from two interfering pathways: (i) absorption of both harmonic $2q-1$ and an IR photon and (ii) absorption of harmonic $2q+1$ and stimulated emission of an IR photon. Therefore, the intensity of each sideband, on each side of the molecule, oscillates at a $2\omega_0$ frequency when scanning $\tau_{\text{XUV-IR}}$ [7].

As an illustration, Fig. 4 shows the SB_{22} RABBIT spectra obtained with a standard fundamental photon energy of $\omega_0 = 1.55\,\text{eV}$, which corresponds to a wavelength $\lambda_0 = 2\pi c/\omega_0 = 800$ nm (c is the light velocity). Figures 4(a) and 4(b) display the spectra obtained on the left and right sides of the molecule,

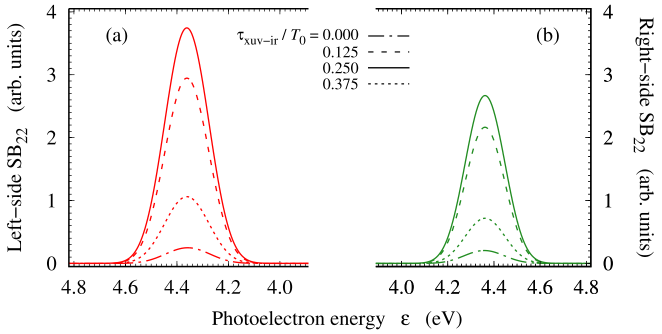

FIG. 4. Orientation-resolved SB$_{22}$ towards the (a) left and (b) right sides of the model molecule, in RABBIT simulations at 800-nm probe wavelength. The spectra are shown for five values of the pump-probe delay $\tau_{\text{XUV-IR}}$ (see inset key) sampling a complete oscillation, see Eq. (8).

respectively, for five values of $\tau_{\text{XUV-IR}}$ covering a full oscillation in the RABBIT spectrogram. They reveal a clear asymmetry in the overall ionization probability, in favor of the left side (a similar asymmetry is observed in the one-photon case, see the SCWF amplitudes on Fig. 1). They also highlight the typical $\tau_{\text{XUV-IR}}$ dependency of the SB magnitudes inherent to RABBIT, on each side of the molecule.

B. Orientation-resolved molecular phases and delays

Information on the photoemission dynamics are encoded in the phases of the sideband oscillations, the so-called “atomic” (or, here, “molecular”) phases [7]. While the orientation dependency of these oscillations are hardly visible on Fig. 4, we will see that they are significant when interpreted in the time domain at the attosecond scale.

In our simulations, orientation-resolved molecular phases $\vartheta(\theta_\text{k})$ were extracted from the photoelectron spectra by fitting the interferometric pattern function [7]

$$f(\tau_{\text{XUV-IR}}) = P(\theta_\text{k}) + Q(\theta_\text{k})\cos[2\omega_0 \times \tau_{\text{XUV-IR}} - \vartheta(\theta_\text{k})] \quad (8)$$

to the spectrally integrated intensity of each sideband on each side of the molecule ($\theta_\text{k} = 0^\circ, 180^\circ$). All the θ_k-dependent quantities play the role of fitting parameters.

Various schemes were developed over the past years to analyze these phases in the time domain, see, e.g., the reviews [40,41]. Our present study focuses on the orientation-resolved “molecular delays” defined as

$$\tau_{\text{mol}}(\theta_\text{k}) = \frac{\vartheta(\theta_\text{k})}{2\omega_0}. \quad (9)$$

They express the angular variations of the so-called “atomic’ (or “molecular”) delays that were first introduced to interpret RABBIT experiments in terms of photoemission dynamics [4].

We first present and analyze the results obtained with the standard fundamental wavelength, $\lambda_0 = 800$ nm. We considered odd harmonic orders ranging from 21 to 29, producing sideband photoelectrons near threshold ($\varepsilon < 15$ eV). The orientation-resolved molecular delays on the left and right sides of the molecule are displayed in Figs. 5(a) and 5(b), respectively (circles connected by dash-dotted guidelines, see wavelength labels). Their overall trend is typical of molecular delays in smooth continua, their magnitude decaying monotonically when the sideband energy increases. Their values lie in the 100 as range, with a relatively small anisotropy, which remarkably contrasts with the much shorter one-photon counterparts displayed in Fig. 2. The anisotropy is nevertheless significant at the attosecond timescale, consistently with previous experimental and theoretical studies [24–26,31]. This can be seen in Fig. 6 where the stereo molecular delays

$$\Delta\tau_{\text{mol}} = \tau_{\text{mol}}(180^\circ) - \tau_{\text{mol}}(0^\circ) \quad (10)$$

are plotted (same legend). Ranging within a few tens of as at the lowest considered sideband, the magnitude of $\Delta\tau_{\text{mol}}$ also follows a global decaying trend when ε increases.[3] They also significantly differ from the stereo Wigner delays computed

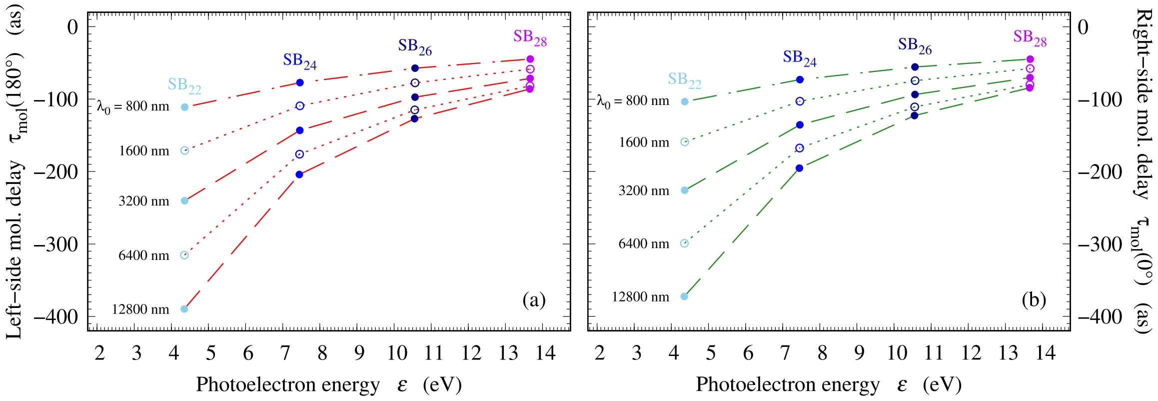

FIG. 5. Orientation-resolved molecular delays [Eq. (9)] measured on the (a) left and (b) right sides of the molecule as a function of the average sideband energy. The data were obtained in a series of RABBIT simulations with various “probe” wavelength values (see labels). The actual data, shown as symbols, are connected with guidelines for each value of λ_0 (with alternating line styles). For simplicity, the sideband labels are displayed for the standard 800-nm case only (dashed-dotted lines).

---

[3] That trend is not necessarily monotonic, e.g., for $\lambda_0 = 800$ nm the delay changes sign around SB$_{28}$.

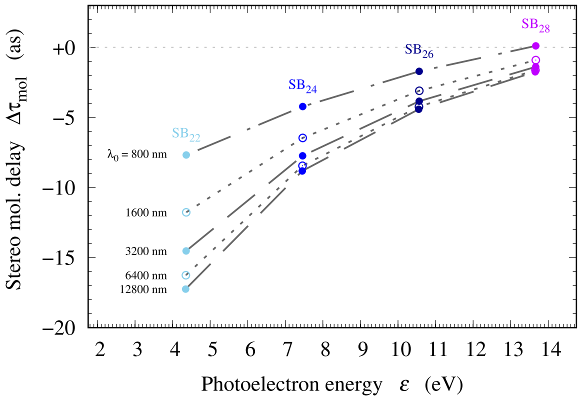

FIG. 6. Stereo molecular delays $\Delta\tau_{\mathrm{mol}}$ [Eq. (10)] as a function of the average sideband energy, computed for a set of λ_0 values in RABBIT simulations, see caption of Fig. 5.

at $x_{\mathrm{ref}} = \langle x\rangle_0$, in spite of lying within a similar as scale. Note that no alternative choice in the origin provides a satisfactory agreement between the one-photon and two-photon stereo delays with these 800-nm RABBIT simulations, as will be further discussed in Sec. V. As expected and in contrast to the Wigner delays studied in Sec. III, the (orientation-resolved) molecular delays bear no intrinsic dependency with respect to the arbitrary origin x_{ref}. Nevertheless, these measurable quantities depend on the "probe" laser wavelength λ_0 [37,38] We illustrate this in Table II, which displays the values of $\tau_{\mathrm{mol}}(\theta_{\mathrm{k}})$ obtained at $\mathrm{SB}_{\mathrm{n}\times 22}$, on each side of the molecule, when the fundamental wavelength is varied following the geometric progression $2^{n-1} \times 800$ nm ($n = 1$–5).[4] This λ_0 sampling ensures all $\mathrm{SB}_{\mathrm{n}\times 22}$ sidebands to be centered at the same photoelectron energy than SB_{22} for the 800-nm case ($\varepsilon = 4.35$ eV). It thus allows assessing the evolution of $\tau_{\mathrm{mol}}(\theta_{\mathrm{k}})$ with respect to λ_0 solely. Indeed, we observe here that the orientation-resolved molecular delays depend significantly on λ_0. That dependency is not only the result of the division by ω_0 on the right-hand side (r.h.s.) of Eq. (9) since the orientation-resolved molecular phases $\vartheta(\theta_{\mathrm{k}})$ themselves depend on λ_0 in an antagonist way (see the same table and the above-mentioned references).

The data obtained for higher sideband orders $\mathrm{SB}_{\mathrm{n}\times(2\mathrm{q}+1)}$ with the same set of wavelengths are also displayed in Figs. 5 and 6. The conclusions regarding the λ_0 dependency are the same as for $\mathrm{SB}_{\mathrm{n}\times 22}$. Focusing on that dependency, one should note that the orientation-resolved delay $\tau_{\mathrm{mol}}(\theta_{\mathrm{k}})$ associated with each sideband energy, on each side of the molecule, follows an apparent logarithmic trend with respect to λ_0 [in Fig. 5, for each $\mathrm{SB}_{\mathrm{n}\times 2\mathrm{q}}$, the values of $\tau_{\mathrm{mol}}(\theta_{\mathrm{k}})$ are ∼ evenly spaced while λ_0 follows a geometric progression]. As will be discussed in Sec. V, this is consistent with previous studies and state of the art analytical derivations. However, the λ_0 dependency *of their angular variations*, namely, of the stereo molecular delays $\Delta\tau_{\mathrm{mol}}$ at fixed ε, is no longer logarithmic (see Fig. 6). Strikingly, it instead appears to be converging when λ_0 increases.

TABLE II. Orientation-resolved molecular phases $\vartheta(\theta_{\mathrm{k}})$ and delays $\tau_{\mathrm{mol}}(\theta_{\mathrm{k}})$ [Eq. (9)] associated with $\mathrm{SB}_{\mathrm{n}\times 22}$ for five values of the fundamental wavelength λ_0, $2^{n-1} \times 800$ nm ($n = 1$–5). These sidebands share the same average photoelectron energy $\varepsilon = 4.35$ eV.

λ_0 (nm)	800	1600	3200	6400	12 800
$\vartheta(0^\circ)$ (rad)	−0.4872	−0.3747	−0.2661	−0.1762	−0.1097
$\vartheta(180^\circ)$ (rad)	−0.5234	−0.4024	−0.2831	−0.1858	−0.1148
$\tau_{\mathrm{mol}}(0^\circ)$ (as)	−103.4	−159.0	−225.8	−299.0	−372.6
$\tau_{\mathrm{mol}}(180^\circ)$ (as)	−111.0	−170.8	−240.3	−315.4	−389.8

In the next section, we investigate numerically the link between the fundamental stereo Wigner delays and the measurable stereo molecular delays, by addressing the ways to account for the dependencies pertaining to each of them.

V. RABBIT AS A PUMP-PROBE SCHEME TO MEASURE WIGNER DELAYS

When the RABBIT technique is used to investigate the dynamics of photoemission in terms of Wigner delays [4], it is seen as an interferometric pump-probe scheme where the XUV harmonic pulse initiates single-photon ionization processes that are probed by the fundamental field at λ_0 (typically in the IR domain). Within this paradigm, atomic (or molecular) delays are considered as measurements of Wigner delays, modified by a correction term resulting from the IR probe stage. Retrieving the first out of the second thus requires the knowledge of the probe term, as introduced in Ref. [4]. Here, we will see that the asymmetry of our model molecule induces angular variations of the molecular-Wigner delay differences that are significant on the attosecond scale.

Using the orientation-dependent delays introduced in the previous sections, we define here the orientation-resolved probe delay as

$$\tau_{\mathrm{probe}}(\theta_{\mathrm{k}}) = \tau_{\mathrm{mol}}(\theta_{\mathrm{k}}) - \tau_{\mathrm{w}}(\theta_{\mathrm{k}}). \tag{11}$$

Below, we confront our orientation-averaged results to an available analytic model, before focusing on the details of their angular variations.

A. Orientation averaged delays

A convenient closed-form expression modeling the λ_0 dependency of this correction was derived using asymptotic expansions and well-delineated approximations, see [38,45]. With the notations of the present paper, it reads

$$g_\varepsilon(\lambda_0) = \frac{Z}{(2\varepsilon)^{3/2}}[2 - \ln(\varepsilon c\lambda_0)]. \tag{12}$$

Z is, in principle, the charge associated with the asymptotic Coulomb field felt by the photoelectron, but it can also be used

---

[4] Results for the largest considered wavelength (12 800 nm) were obtained using second-order perturbation theory rather than by solving the TDSE to avoid numerical issues related to the tight spectral proximity of the photoelectron peaks.

TABLE III. Effective charge obtained by fitting the average probe delay $\bar{\tau}_{\text{probe}}$ [Eq. (13)] with the formula given in Eq. (12), as a function of λ_0 at fixed ε for each series of sidebands $\text{SB}_{\text{n}\times 2\text{q}}$ (n parametrizes the λ_0 sampling, see caption of Table II). The standard relative error for each fit is indicated in brackets.

$2q$:	22	24	26	28
Z [err]:	0.80 [2%]	0.84 [2%]	0.85 [3%]	0.84 [5%]

as an adjustable parameter compensating for some approximations. This formula and related ones (see also Ref. [37]) are commonly exploited as such in experimental and theoretical studies, see, e.g., Refs. [14,17,26,33].

The function given in Eq. (12) notably underlines the overall logarithmic λ_0 dependency of the molecular delays, anticipated earlier when commenting our results displayed in Fig. 5. In addition, it refers to Wigner delays defined with Coulomb reference waves, which is the natural choice for photoemission. However, it is an isotropic expression.[5] Hence, it cannot account for orientation-resolved measurements that reveal angular variations of the probe term, as, e.g., experimentally in He [25] and theoretically in noble gas atoms [27], as well as in the present simulations, as developed below.

To assess the relevance of $g_\varepsilon(\lambda_0)$ in the context of the present work, we fitted it to the orientation-averaged probe delays obtained in our numerical experiments

$$\bar{\tau}_{\text{probe}} = \frac{1}{2} \sum_{\theta_{\text{k}}=0^\circ,180^\circ} \tau_{\text{probe}}(\theta_{\text{k}}), \tag{13}$$

using the effective charge Z as the sole fitting parameter. Note that the average value $\bar{\tau}_{\text{probe}}$ does *not* depend on the origin x_{ref} in contrast to the orientation-resolved counterpart $\tau_{\text{probe}}(\theta_{\text{k}})$.[6] Indeed, the correction term inherited from $\tau_{\text{w}}(\theta_{\text{k}})$, modeled by Eq. (5), cancels out when averaging over θ_{k} (this can be verified, e.g., with the data of Table I).

The fit was done independently for each sideband series $\text{SB}_{\text{n}\times 2\text{q}}$, each of them corresponding to a fixed photoelectron energy ε. The four series provide consistent Z values, lying around 0.83 within the standard error of the fits ($\lesssim 5\%$), see Table III. The average probe term $\bar{\tau}_{\text{probe}}$ is displayed against λ_0 in Fig. 7, for the four considered series of sidebands. The fits, displayed on the same figure, appear to accurately follow the orientation-averaged numerical data, within the timescale of the plot.

We will now take a closer look at the angular variations of the probe delay which are not taken into account by the analytic model function $g_\varepsilon(\lambda_0)$, but nevertheless manifest at the attosecond timescale [34].

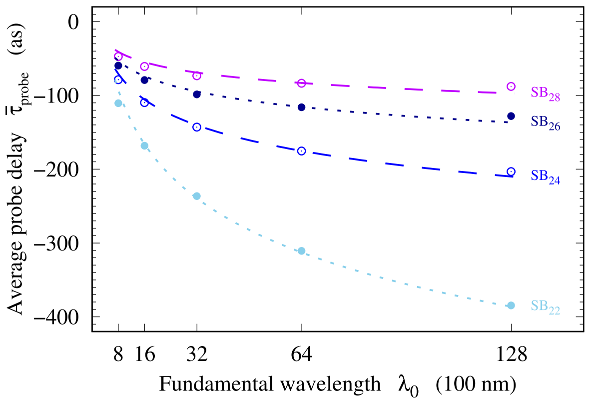

FIG. 7. Average probe delay against the RABBIT probe wavelength λ_0. Numerical results [Eq. (13)] are displayed as circles. Alternating dashed and dotted lines correspond to the universal closed-form expression [Eq. (12)], where Z was used as a fitting parameter, see Table III. The results are displayed for the four sideband datasets considered all through the paper. For simplicity, each set is labeled with the sideband order in the 800-nm case.

B. Reconciliating orientation-resolved molecular and Wigner delays

We eventually address the angular variation

$$\Delta\tau_{\text{probe}} = \tau_{\text{probe}}(180^\circ) - \tau_{\text{probe}}(0^\circ) \tag{14}$$

$$= \Delta\tau_{\text{mol}} - \Delta\tau_{\text{w}}, \tag{15}$$

hereafter referred to as the stereo probe delay. In contrast to the orientation-resolved or -averaged probe delays, it is not affected by the choice of the reference-wave used to define the Wigner delays. Instead, it inherits the origin dependency of the Wigner delay, see Sec. III, and the wavelength-dependency of the molecular delay, see Sec. IV and above.

The values of $\Delta\tau_{\text{probe}}$ obtained in our simulations are shown in Fig. 8 against the photoelectron energy ε. Figures 8(a) to 8(c) correspond to a given probe wavelength λ_0 value $2^{(n-1)} \times 800$ nm ($n = 1, 3, 5$). We performed a systematic scan of x_{ref} and only show a selection of representative cases (each guideline corresponds to a given value of x_{ref}).[7]

Looking at Fig. 8(a), one can see that at 800 nm no x_{ref} value allows the stereo probe delay to vanish at all energies: the arbitrary coordinate origin $x_{\text{ref}} = 0$ and the initial average position $x_{\text{ref}} = \langle x \rangle_0$ [$= -0.16$ Å, see Eq. (7)] making no exception. At this point, one may conclude that standard RABBIT measurements cannot provide arbitrarily accurate access to the angular variations of Wigner delays in molecular photoemission.

---

[5] Its isotropy comes from the hypothesis according to which the λ_0 field probes the photoelectron outside the system- and channel-specific short-range interaction zone, i.e., where it feels only the universal (isotropic) Coulomb tail of the ionic potential.

[6] This is consistent with the results obtained in [14], where orientation-averaged simulations reached a satisfactory agreement with experiments without considering the origin issue.

[7] We checked that the finite-difference approximation

$$\left.\frac{\partial\eta}{\partial\varepsilon}\right|_{\varepsilon_{2q}} \simeq \frac{\eta(\varepsilon_{2q}+\omega_0) - \eta(\varepsilon_{2q}-\omega_0)}{2\omega_0}, \tag{16}$$

which underlies any attempt to link the atomic or molecular phases to the Wigner delays [4], remains accurate in all the considered cases. In the most pathological situation, i.e., at the lowest considered energy probed with the largest laser frequency ω_0 (SB_{22} at 800 nm), this approximation induces an error of few 0.1 as.

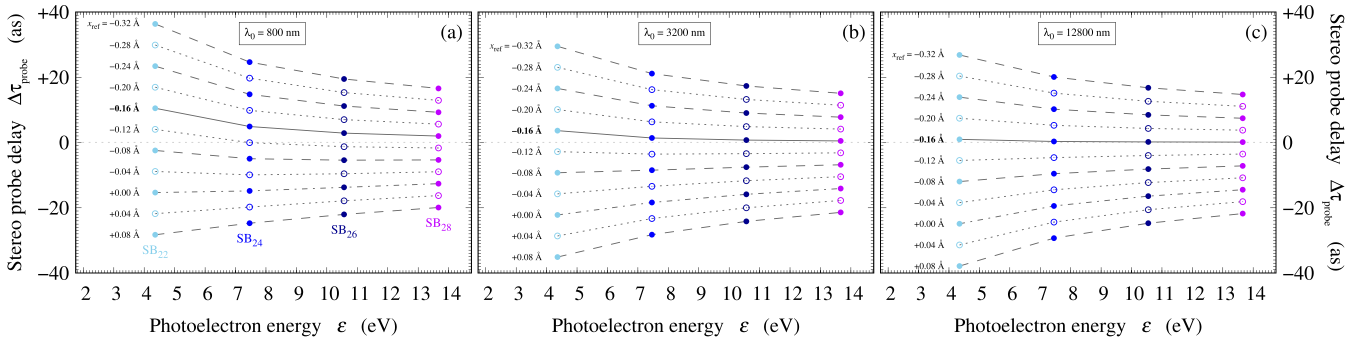

FIG. 8. Stereo correction delay $\Delta\tau_{\text{probe}}$ [Eq. (14)] as function of the photoelectron energy ε. Each panel [(a)–(c)] corresponds to a given value of λ_0 used to measure the molecular delays. The data, shown as alternating filled and empty circles connected with guidelines, were computed at the energies of the sidebands considered in the RABBIT simulations. Each line corresponds to a given value of x_{ref} used to define and compute the Wigner delays. Solid lines correspond to the datasets obtained with $x_{\text{ref}} = \langle x\rangle_0 = -0.16$ Å, which converge to 0 at all energies when λ_0 increases. Dash-dotted lines correspond to the datasets obtained with the arbitrary origin $x_{\text{ref}} = 0$. For simplicity, the sidebands are labeled for the (a) 800-nm case only.

However, the results obtained at larger wavelengths single out the average initial position $\langle x\rangle_0$ as a specific x_{ref} origin for which $\Delta\tau_{\text{probe}}$ does strikingly vanish at all energies, when λ_0 increases. This observation eventually comforts the idea that RABBIT virtually probes molecular photoemission dynamics with high accuracy. It also confirms the average initial electron position as a statistically representative parameter implicitly characterizing the dynamics studied by such experiments, as assumed in Ref. [31].

On the theory side, it provides an objective criterion for setting the electron position origin in anisotropic scattering delays computations. It is important here to keep in mind that $\Delta\tau_{\text{probe}}$ as such [Eq. (11)] is not an experimentally measurable quantity. Its x_{ref} dependency directly issues from the *definition* of the term $\Delta\tau_{\text{w}}$ and has nothing to do with the *measurement* of the term $\Delta\tau_{\text{mol}}$. Significant values of $\Delta\tau_{\text{probe}}$ at large photoelectron energies are thus spurious signatures of an inappropriate reference position in the theoretical definitions of the (stereo) Wigner delay. They are therefore related to an ill-defined clock rather than to a physically relevant asymmetry in the photoemission dynamics. In contrast, nonzero $\Delta\tau_{\text{w}}$ persisting at low energies in standard 800-nm RABBIT measurements (even though the position origin is properly set) are signatures of the asymmetric probe influence on the measurements. They however vanish when the probe wavelength increases.

Hence, stereo Wigner delays are encoded in RABBIT measurements with attosecond resolution, when the position origin is properly set and in the limit of a vanishing probe frequency, or at sufficiently large photoelectron electron energies.[8] Their angular variations are related to differences in the potential energy landscape explored by the photoelectron while escaping the molecule in one direction or the other, and cannot be directly related to the "technical", potential-independent, correction given in Eq. (5). This partly contradicts the interpretations of the authors of Refs. [31,34], without questioning the main conclusions of these studies.

On the experimental side, the probe wavelengths cannot be arbitrarily increased in practice as it is done in the present simulations. The question of the magnitude of $\Delta\tau_{\text{probe}}$ thus remains to be dealt with, even when properly setting the position origin.[9] That magnitude is expected to highly depend on the degree of asymmetry of the probed molecule, among other things. Deriving a universal λ_0- and ε-dependent model formula for $\Delta\tau_{\text{probe}}$ is beyond the scope of the present paper. In this last part, we will review what can be learned from our simulations with respect to this probe term.

First, one should note that, in the present case, $\Delta\tau_{\text{probe}}$ is relatively small, even for $\lambda_0 = 800$ nm. In the considered near-threshold energy range, it hardly exceeds 10 as around 4 eV and then decays monotonically, reaching ~2 as before 14 eV. We can thus expect the stereo probe delay to quickly reach the sub-as timescale, which should make it negligible when considering photoemission at much higher energies and when the molecular asymmetry is not too pronounced. This includes the results published in Ref. [24] where stereo Wigner delays were investigated numerically in the context of streaking rather than RABBIT. As mentioned earlier in the Introduction, these results show no significant difference between the Wigner and streaking delays beyond ~20 eV.

We also investigated the evolution of $\Delta\tau_{\text{probe}}$ against the probe wavelength, for each of the considered photoelectron energies. The results are displayed in Fig. 9. The striking alignments of the data, for each energy, in this log-log plot suggest a general λ_0 dependency following simple decaying power laws, as confirmed by fitting the data with a λ_0^{-p} law. We obtained p values around 1 slowly increasing with the photoelectron energy, see Table IV. We performed additional 3D simulations on the H atom (not shown here), where we measured orientation-resolved atomic delays with RABBIT. We found that their angular variations, when they are significant, also display λ_0 dependencies following similar power

---

[8] We reproduced the stereo Wigner delays displayed in Fig. 9(a) of Ref. [34] and verified that a proper correction of the origin brings the data significantly closer to the 800-nm- RABBIT delays reported in the same figure, in particular, at large energies.

[9] All through the remainder of the paper the choice $x_{\text{ref}} = \langle x\rangle_0$ is assumed.

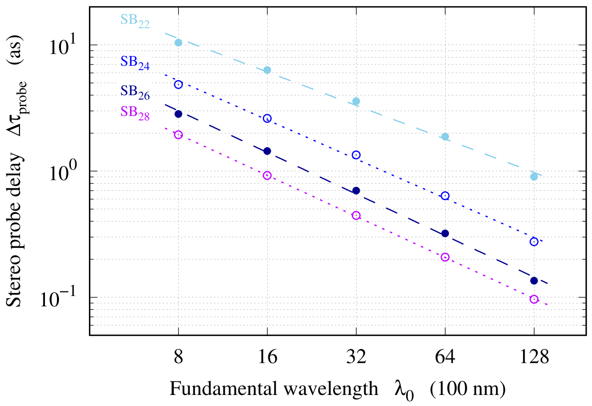

FIG. 9. Stereo probe delay [Eq. (14)] as a function of the probe wavelength λ_0, for each set of sidebands centered at a given energy (each set is labeled with the sideband order of the 800-nm case). The numerical data obtained in our simulations are indicated as symbols (same legend as in Fig. 7). The fits of the function $h(\lambda_0) = a \times \lambda_0^{-p}$ to each set of data are shown as lines (alternating dashed and dotted styles). The fitted values of the exponent p are provided in Table IV. The plot is displayed in a log-log scale.

laws, which stabilize when λ_0 increases, towards exponent values within ~0.75–1.5 depending on the orientation. In that case, the angular (momentum) dependency of the probe delay term is attributed to the ℓ-dependent $\sim 1/r^2$ centrifugal barrier [28], the plain atomic potential being otherwise spherically symmetric. We also performed an equivalent study on the asymmetric 1D model molecule used in Ref. [34]. We could fit the stereo probe delay to the λ_0^{-p} law with very high accuracy, with exponent values within 0.8–0.9 in the same energy range. We eventually considered a more pathological case, provided by the asymmetric 1D model molecule of Ref. [42]. Its potential is composed of a single soft-Coulomb well augmented with a barrier on one side only (see Fig. 3 of Ref. [42]). Its ground state is essentially symmetric, while the barrier induces relatively large stereo-Wigner delays in the 100-as range a few eV above the ionization threshold. Here, the obtained stereo probe delay follow a λ_0^{-p} law with a lower and variable accuracy, and a broader dispersion of p values (up to 2). We could partly relate the inaccuracies of the fits to the pronounced spectral variations of the scattering phase shifts, implying a breakdown of the finite difference approximation needed to relate the RABBIT molecular delays to the Wigner delays, see footnote 7 on p. 16.

These empirical, numerical findings suggest the existence of an underlying analytical law for the angular variations of $\Delta\tau_{\text{probe}}$ depending on the molecule asymmetry, the photoelectron energy, and the probe laser wavelength. Such an analytical law remains to be established.

TABLE IV. Power laws obtained by fitting the stereo probe delay $\Delta\tau_{\text{probe}}$ [Eq. (14)] with $h(\lambda_0) = a \times \lambda_0^{-p}$, at fixed ε for each series of sidebands $\text{SB}_{n\times 2q}$ (n parametrizes the λ_0 sampling, see caption of Table II). The standard relative error for each fit is indicated in brackets.

$2q$:	22	24	26	28
p [err]:	0.88 [5%]	1.03 [4%]	1.09 [3%]	1.08 [1%]

VI. SUMMARY AND CONCLUSION

Using numerical experiments, we reviewed the physics underlying the concepts of Wigner delay that characterize single-photon ionization processes and of so-called atomic or molecular delay inferred from RABBIT measurements, their interpretations and their connections.

The simulations were performed on a simple 1D asymmetric model molecule, with a particular focus on the angular variations of the delays with respect to the photoelectron ejection direction and on the intrinsic dependencies of the delays with respect to theoretical and experimental parameters.

We verified that our orientation-averaged results are consistent with an available analytical formula [38] for the difference between the molecular and Wigner delays. By construction, that formula accounts for the wavelength dependency of the molecular delay on the one hand and for the specific choice of Coulomb reference waves to define and compute the Wigner delays on the other hand. However, it is an isotropic formula that cannot account for the angular variations of the molecular and Wigner delays nor of their differences.

Addressing this issue puts forward the intrinsic dependency of the orientation-resolved Wigner delays with respect to an arbitrary electron position origin, which does not concern molecular delays. Our simulations, however, show that orientation-resolved molecular phases and Wigner delays can be related, when and only when the latter is defined with a *specific origin corresponding to the average electron position in the initial bound state*. This demonstrates empirically that the initial average electron position is encoded in RABBIT measurements and thus provides an unambiguous prescription for setting the electron position origin in the definition and computation of orientation-resolved Wigner delays. A different position origin, when not corrected, can lead to dramatically and spuriously large delays even when it is set "within" the molecule, i.e., a few tenths of Å from the average initial position. The magnitude of such artificially enhanced delays is then likely to hide the actual, physically relevant, anisotropic dynamics occurring at the attosecond scale.

Moreover, our simulations reveal angular variations of the molecular delays matching those of the Wigner delays *in the limit of a vanishing RABBIT probe frequency*. The wavelengths considered in our simulations extend way beyond those routinely available in real-life experiments. However, the differences observed even at 800 nm are rather small. They also decay rapidly when the photoelectron energy increases. Therefore, one can expect them to be negligible in many practical cases, depending on the photoelectron energy and the degree of asymmetry of the molecule. Finally, the observed trend with respect to λ_0 will serve as a basis for further analytical developments in view to include a proper angular dependency in the probe term, also with more elaborate field configurations [46–49]. This will allow observing the dynamics of a most fundamental quantum process in all its complexity, with actual attosecond accuracy.

ACKNOWLEDGMENTS

The authors acknowledge fruitful and stimulating discussions with Pascal Salières and Bernard Pons. This research received the financial support of the French National Research Agency through Grants No. ANR-15-CE30-0001-CIMBAAD and No. ANR-20-CE30-0007-DECAP.

APPENDIX: PARTIAL-WAVE EXPANSION IN 1D

1. 1D polar coordinates

In 1D, position is commonly characterized by a single coordinate $z \in \mathbb{R}$. Alternatively, it can be expressed via a set of two "polar" coordinates consisting in

$$\begin{aligned} &\text{a radial coordinate } r = |z| \ (r \in \mathbb{R}^+),\\ &\text{an angular coordinate } \theta = \arccos(z/|z|) \ (\theta \in \{0, \pi\}). \end{aligned} \tag{A1}$$

In spite of being unusual, this representation is of interest to highlight existing analogies between 1D scattering problems [43,50] and problems in higher dimensions where partial-wave expansions are standard.

2. Angular basis functions

In analogy with 3D spherical harmonics, let us introduce the following set of basis functions:

$$Y_\ell(\theta) = \frac{1}{\sqrt{2}}\cos^\ell\theta,\ \ell \in \{0, 1\} \tag{A2}$$

for the discrete angular coordinate θ introduced in Eq. (A1). Defined as such, the functions are orthogonal and normalized to unity

$$(Y_\ell|Y_{\ell'}) = \delta_{\ell\ell'}, \tag{A3}$$

where δ is the Kronecker symbol and the (|) bra-ket notation refers to the scalar product with respect to the angular variable

$$(A|B) = \sum_{\theta=0,\pi} [A(\theta)]^\star B(\theta). \tag{A4}$$

The two functions further verify the following composition rule:

$$Y_\ell(\theta)Y_{\ell'}(\theta) = \sqrt{2}[\delta_{\ell\ell'} \times Y_0(\theta) + (1 - \delta_{\ell\ell'}) \times Y_1(\theta)]. \tag{A5}$$

One must note that the values assigned to the index ℓ are arbitrary. In particular, this "quantum number" cannot be associated with an angular momentum since the angular coordinate is not continuous (see Noether's theorem [51]), i.e., rotation is not defined in one dimension. However, it is related to the parity properties of 1D functions, as exploited in the following.

3. Partial waves

The even (f_0) and odd (f_1) components of any function F can be defined as

$$f_\ell(r) = \frac{1}{\sqrt{2}}[F(r) + (-1)^\ell F(-r)] \tag{A6}$$

for all $r \in \mathbb{R}^+$. The normalization factor $1/\sqrt{2}$ is here introduced such that $F(z)$ expressed with the (r, θ) coordinates takes the simple form of a partial-wave expansion

$$F(z) = \sum_{\ell=0,1} f_\ell(r)Y_\ell(\theta). \tag{A7}$$

Hence, $Y_0(\theta)$ corresponds to the angular part of an even function of z and $Y_1(\theta)$ to the one of an odd function.

4. Schrödinger equation

We consider the time-independent Schrödinger equation

$$\left[-\frac{1}{2}\frac{d^2}{dz^2} + V(z) - \varepsilon\right]\Psi(z) = 0, \tag{A8}$$

of a 1D particle (of mass equal to 1) with total energy ε, where the 1D partial-wave expansions of the potential and of the solution wave function read

$$V(z) = \sum_{\ell=0,1} v_\ell(r)Y_\ell(\theta), \tag{A9}$$

$$\Psi(z) = \sum_{\ell=0,1} \psi_\ell(r)Y_\ell(\theta). \tag{A10}$$

Projecting the Schrödinger equation [Eq. (A8)] on the angular basis $\{Y_0(\theta), Y_1(\theta)\}$, and using Eqs. (A3), (A6), and

$$\left(Y_\ell\middle|\frac{d^2}{dz^2}\middle|Y_{\ell'}\right) = \delta_{\ell\ell'}\frac{d^2}{dr^2}, \tag{A11}$$

one gets the following coupled equations for the radial functions $\psi_\ell(r)$:

$$\left[-\frac{1}{2}\frac{d^2}{dr^2} + v_0(r) - \varepsilon\right]\psi_\ell(r) + v_1(r)\psi_{1-\ell}(r) = 0, \tag{A12}$$

where the odd component of the potential $v_{-1}(r)$ is responsible for the coupling between the two partial waves $\psi_0(r)$ and $\psi_1(r)$.

The continuity conditions of the solution wave function $\Psi(z)$ translate into the following boundary conditions at the origin:

$$\psi_0'(0) = 0, \tag{A13}$$

$$\psi_1(0) = 0, \tag{A14}$$

to be imposed when implementing the numerical resolution of the system [Eq. (A12)]. In the doubly degenerate continuum, two linearly independent wave functions can be obtained by solving the system with two linearly independent arbitrary sets of initial conditions $\{\psi_0(0), \psi_1'(0)\}$.

[1] A. L. Cavalieri, N. Muller, T. Uphues, V. S. Yakovlev, A. Baltuška, B. Horvath, B. Schmidt, L. Blumel, R. Holzwarth, S. Hendel, M. Drescher, U. Kleineberg, P. M. Echenique, R. Kienberger, F. Krausz, and U. Heinzmann, Attosecond spectroscopy in condensed matter, Nature (London) **449**, 1029 (2007).

[2] M. Schultze, M. Fieß, N. Karpowicz, J. Gagnon, M. Korbman, M. Hofstetter, S. Neppl, A. L. Cavalieri, Y. Komninos, T. Mercouris, C. A. Nicolaides, R. Pazourek, S. Nagele, J. Feist, J. Burgdörfer, A. M. Azzeer, R. Ernstorfer, R. Kienberger, U. Kleineberg, E. Goulielmakis, F. Krausz, and V. S. Yakovlev, Delay in photoemission, Science **328**, 1658 (2010).

[3] S. Haessler, B. Fabre, J. Higuet, J. Caillat, T. Ruchon, P. Breger, B. Carré, E. Constant, A. Maquet, E. Mével, P. Salières, R. Taïeb, and Y. Mairesse, Phase-resolved attosecond near-threshold photoionization of molecular nitrogen, Phys. Rev. A **80**, 011404(R) (2009).

[4] K. Klünder, J. M. Dahlström, M. Gisselbrecht, T. Fordell, M. Swoboda, D. Guénot, P. Johnsson, J. Caillat, J. Mauritsson, A. Maquet, R. Taïeb, and A. L'Huillier, Probing single-photon ionization on the attosecond time scale, Phys. Rev. Lett. **106**, 143002 (2011).

[5] E. P. Wigner, Lower limit for the energy derivative of the scattering phase shift, Phys. Rev. **98**, 145 (1955).

[6] H. G. Muller, Reconstruction of attosecond harmonic beating by interference of two-photon transitions, Appl. Phys. B **74**, s17 (2002).

[7] V. Véniard, R. Taïeb, and A. Maquet, Phase dependence of $(N+1)$-color $(N > 1)$ ir-uv photoionization of atoms with higher harmonics, Phys. Rev. A **54**, 721 (1996).

[8] P. M. Paul, E. S. Toma, P. Breger, G. Mullot, F. Augé, P. Balcou, H. G. Muller, and P. Agostini, Observation of a train of attosecond pulses from high harmonic generation, Science **292**, 1689 (2001).

[9] Y. Mairesse, A. de Bohan, L. J. Frasinski, H. Merdji, L. C. Dinu, P. Monchicourt, P. Breger, M. Kovačev, R. Taïeb, B. Carré, H. G. Muller, P. Agostini, and P. Salières, Attosecond synchronization of high-harmonic soft x-rays, Science **302**, 1540 (2003).

[10] M. Hentschel, R. Kienberger, C. Spielmann, G. A. Reider, N. Milosevic, T. Brabec, P. Corkum, U. Heinzmann, M. Drescher, and F. Krausz, Attosecond metrology, Nature (London) **414**, 509 (2001).

[11] F. Krausz and M. Ivanov, Attosecond physics, Rev. Mod. Phys. **81**, 163 (2009).

[12] P. Salières, A. Maquet, S. Haessler, J. Caillat, and R. Taïeb, Imaging orbitals with attosecond and Ångström resolutions: toward attochemistry? Rep. Prog. Phys. **75**, 062401 (2012); I. C. D. Merritt, D. Jacquemin, and M. Vacher, Attochemistry: Is controlling electrons the future of photochemistry? J. Phys. Chem. Lett. **12**, 8404 (2021); F. Calegari and F. Martiín, Open questions in attochemistry, Commun. Chem. **6**, 184 (2023).

[13] T. Barillot, C. Cauchy, P.-A. Hervieux, M. Gisselbrecht, S. E. Canton, P. Johnsson, J. Laksman, E. P. Mansson, J. M. Dahlström, M. Magrakvelidze, G. Dixit, M. E. Madjet, H. S. Chakraborty, E. Suraud, P. M. Dinh, P. Wopperer, K. Hansen, V. Loriot, C. Bordas, S. Sorensen, and F. Lépine, Angular asymmetry and attosecond time delay from the giant plasmon resonance in C_{60} photoionization, Phys. Rev. A **91**, 033413 (2015).

[14] M. Huppert, I. Jordan, D. Baykusheva, A. von Conta, and H. J. Wörner, Attosecond delays in molecular photoionization, Phys. Rev. Lett. **117**, 093001 (2016).

[15] A. W. Bray, F. Naseem, and A. S. Kheifets, Photoionization of Xe and Xe@C_{60} from the $4d$ shell in RABBITT fields, Phys. Rev. A **98**, 043427 (2018).

[16] H. Ahmadi, E. Plésiat, M. Moioli, F. Frassetto, L. Poletto, P. Decleva, C. D. Schrötter, T. Pfeifer, R. Moshammer, A. Palacios, F. Martín, and G. Sansone, Attosecond photoionisation time delays reveal the anisotropy of the molecular potential in the recoil frame, Nat. Commun. **13**, 1242 (2022).

[17] A. Boyer, S. Nandi, and V. Loriot, Attosecond probing of photoionization dynamics from diatomic to many-atom molecules, Eur. Phys. J. Spec. Top. **232**, 1 (2023).

[18] X. Gong, E. Plésiat, A. Palacios, S. Heck, F. Martín, and H. J. Wörner, Attosecond delays between dissociative and nondissociative ionization of polyatomic molecules, Nat. Commun. **14**, 4402 (2023).

[19] A. Thuppilakkadan, S. Banerjee, and H. R. Varma, Modifications in the angular photoemission time delay in Ar@$C_{60}^{q=-1}$: Coulomb confinement resonance as an amplifier of the spin-orbit-interaction-activated interchannel coupling effect, Phys. Rev. A **107**, 052804 (2023).

[20] S. Beaulieu, A. Comby, A. Clergerie, J. Caillat, D. Descamps, N. Dudovich, B. Fabre, R. Géneaux, F. Légaré, S. Petit, B. Pons, G. Porat, T. Ruchon, R. Taïeb, V. Blanchet, and Y. Mairesse, Attosecond-resolved photoionization of chiral molecules, Science **358**, 1288 (2017).

[21] P. Hockett, E. Frumker, D. M. Villeneuve, and P. B. Corkum, Time delay in molecular photoionization, J. Phys. B: At., Mol. Opt. Phys. **49**, 095602 (2016).

[22] R. Zhang, F. Wang, Q. Liao, and P. Lu, Role of molecular alignment in attosecond photoionization of N_2, Phys. Rev. A **108**, 013113 (2023).

[23] Q. Ke, Y. Zhou, Y. Liao, M. Li, K. Liu, and P. Lu, Spheroidal-wave analysis of time delay in molecular reconstruction of attosecond beating by interference of two-photon transitions around a cooper-like minimum, Phys. Rev. A **108**, 013112 (2023).

[24] A. Chacon, M. Lein, and C. Ruiz, Asymmetry of Wigner's time delay in a small molecule, Phys. Rev. A **89**, 053427 (2014).

[25] S. Heuser, A. Jiménez Galán, C. Cirelli, C. Marante, M. Sabbar, R. Boge, M. Lucchini, L. Gallmann, I. Ivanov, A. S. Kheifets, J. M. Dahlström, E. Lindroth, L. Argenti, F. Martín, and U. Keller, Angular dependence of photoemission time delay in helium, Phys. Rev. A **94**, 063409 (2016).

[26] P. Hockett, Angle-resolved RABBITT: Theory and numerics, J. Phys. B: At., Mol. Opt. Phys. **50**, 154002 (2017).

[27] A. W. Bray, F. Naseem, and A. S. Kheifets, Simulation of angular-resolved RABBITT measurements in noble-gas atoms, Phys. Rev. A **97**, 063404 (2018).

[28] J. Fuchs, N. Douguet, S. Donsa, F. Martïn, J. Burgdörfer, L. Argenti, L. Cattaneo, and U. Keller, Time delays from one-photon transitions in the continuum, Optica **7**, 154 (2020).

[29] C. Cirelli, C. Marante, S. Heuser, C. L. M. Petersson, Á. Jiménez Galán, L. Argenti, S. Zhong, D. Busto, M. Isinger, S. Nandi, S. Maclot, L. Rading, P. Johnsson, M. Gisselbrecht, M. Lucchini, L. Gallmann, J. M. Dahlström, E. Lindroth, A. L'Huillier, F. Martín, and U. Keller, Anisotropic photoemission

time delays close to a Fano resonance, Nat. Commun. **9**, 955 (2018).

[30] D. Trabert, N. Anders, A. Geyer, M. Hofmann, M. S. Schöffler, L. P. H. Schmidt, T. Jahnke, M. Kunitski, R. Dörner, and S. Eckart, Angular dependence of the Wigner time delay upon strong-field ionization from an aligned *p* orbital, Phys. Rev. Res. **5**, 023118 (2023).

[31] J. Vos, L. Cattaneo, S. Patchkovskii, T. Zimmermann, C. Cirelli, M. Lucchini, A. Kheifets, A. S. Landsman, and U. Keller, Orientation-dependent stereo Wigner time delay and electron localization in a small molecule, Science **360**, 1326 (2018).

[32] A. Desrier, Dynamique ultrarapide corrélée : Théorie, simulations et interprétations d'expériences de spectroscopie "attoseconde", Ph.D. thesis, Sorbonne Université, 2018.

[33] X. Gong, W. Jiang, J. Tong, J. Qiang, P. Lu, H. Ni, R. Lucchese, K. Ueda, and J. Wu, Asymmetric attosecond photoionization in molecular shape resonance, Phys. Rev. X **12**, 011002 (2022).

[34] Y. Liao, Y. Zhou, L.-W. Pi, Q. Ke, J. Liang, Y. Zhao, M. Li, and P. Lu, Two-center interference and stereo wigner time delay in photoionization of asymmetric molecules, Phys. Rev. A **104**, 013110 (2021).

[35] A. Maquet, J. Caillat, and R. Taïeb, Attosecond delays in photoionization: Time *and* quantum mechanics, J. Phys. B: At. Mol. Opt. Phys. **47**, 204004 (2014).

[36] J. M. Dahlström, A. L'Huillier, and A. Maquet, Introduction to attosecond delays in photoionization, J. Phys. B: At. Mol. Opt. Phys. **45**, 183001 (2012).

[37] J. Dahlström, D. Guénot, K. Klünder, M. Gisselbrecht, J. Mauritsson, A. L'Huillier, A. Maquet, and R. Taïeb, Theory of attosecond delays in laser-assisted photoionization, Chem. Phys. **414**, 53 (2013).

[38] R. Pazourek, S. Nagele, and J. Burgdörfer, Attosecond chronoscopy of photoemission, Rev. Mod. Phys. **87**, 765 (2015).

[39] L. Cattaneo, J. Vos, M. Lucchini, L. Gallmann, C. Cirelli, and U. Keller, Comparison of attosecond streaking and RABBITT, Opt. Express **24**, 29060 (2016).

[40] M. Vacher, R. Gaillac, A. Maquet, R. Taïeb, and J. Caillat, Transition dynamics in two-photon ionisation, J. Opt. **19**, 114011 (2017).

[41] A. S. Kheifets, Wigner time delay in atomic photoionization, J. Phys. B: At. Mol. Opt. Phys. **56**, 022001 (2023).

[42] R. Gaillac, M. Vacher, A. Maquet, R. Taïeb, and J. Caillat, Attosecond photoemission dynamics encoded in real-valued continuum wave functions, Phys. Rev. A **93**, 013410 (2016).

[43] U. Saalmann and J. M. Rost, Time delays in anisotropic systems, arXiv:2309.02059.

[44] K. C. Kulander, K. J. Schaffer, and J. L. Krause, Time-dependent studies of multiphoton processes, in *Atoms in Intense Laser Fields*, edited by M. Gavrila (Academic, New York, 1992), p. 247.

[45] V. V. Serov, V. L. Derbov, and T. A. Sergeeva, Interpretation of the time delay in the ionization of coulomb systems by attosecond laser pulses, in *Advanced Lasers: Laser Physics and Technology for Applied and Fundamental Science*, edited by O. Shulika and I. Sukhoivanov (Springer, Dordrecht, The Netherlands, 2015), pp. 213–230.

[46] R. Wang, Q. Zhang, C. Cao, M. Li, K. Liu, and P. Lu, Helicity dependent wigner phase shift for photoionization in a circularly polarized laser field, J. Phys. B: At. Mol. Opt. Phys. **55**, 115001 (2022).

[47] D. I. R. Boll, L. Martini, A. Palacios, and O. A. Fojón, Two-color polarization control of angularly resolved attosecond time delays, Phys. Rev. A **107**, 043113 (2023).

[48] A. S. Kheifets and Z. Xu, Polarization control of RABBITT in noble gas atoms, J. Phys. B: At. Mol. Opt. Phys. **56**, 155601 (2023).

[49] M. Han, J.-B. Ji, K. Ueda, and H. J. Wörner, Attosecond metrology in circular polarization, Optica **10**, 1044 (2023).

[50] J. H. Eberly, Quantum scattering theory in one dimension, Am. J. Phys. **33**, 771 (1965); J. Formánek, On phase shift analysis of one-dimensional scattering, *ibid.* **44**, 778 (1976); M. Sassoli de Bianchi, Levinson's theorem, zero-resonances, and time delay in one-dimensional scattering systems, J. Math. Phys. **35**, 2719 (1994); Y. Nogami and C. K. Ross, Scattering from a nonsymmetric potential in one dimension as a coupled-channel problem, Am. J. Phys. **64**, 923 (1996); V. E. Barlette, M. M. Leite, and S. K. Adhikari, Integral equations of scattering in one dimension, *ibid.* **69**, 1010 (2001); L. J. Boya, Quantum-mechanical scattering in one dimension, La Rivista del Nuovo Cimento **31**, 75 (2008); K. I. Elghazawy and C. H. Greene, Wigner time delay in photoionization: A 1D model study, J. Phys. B: At. Mol. Opt. Phys. **56**, 175201 (2023).

[51] H. Goldstein, *Classical Mechanics* (Addison-Wesley, Boston, 1980).